

# A MULTIGRID-BASED APPROACH TO MODELING A HIGH CURRENT SUPERCONDUCTING LINAC FOR WASTE TRANSMUTATION

Paolo Pierini

INFN Milano – LASA, Via Fratelli Cervi, 201, I-20090 Segrate (MI) Italy

## Abstract

High current proton accelerators are nowadays planned for various applications that make use of a large flux of spallation neutrons. The INFN has initiated a study on the conceptual and technical feasibility of a (greater than) 40 MW CW linac for nuclear waste transmutation and energy production.

A safe and reliable operation of these high current machines will require proper control of the beam losses. Accurate simulation codes are needed to assess that the beam losses are maintained to a safe level. As a part of the INFN program, an “ad hoc” code development activity has started, using recent programming techniques and numerical algorithms. The code in development deals, for now, with the proton beam dynamics in the high energy part of the proposed machine, composed by superconducting RF (elliptical) cavities placed between the long drifts of a quadrupole doublet array. The cavities are treated using an on-axis field distribution, either provided in analytical form or as tabular data.

Space charge is evaluated with a fast Poisson solver, that uses a 3D multigrid algorithm. V Cycle or full multigrid algorithms appear to be promising in terms of speed and memory requirements, and can be readily modified for parallel computers. Checks with standard direct point-to-point calculations have been performed.

A major effort has been put in using a modular approach for the data and program design. The code conforms to the F90 syntax and, where possible, makes use of safe programming criteria (controlled scoping of variables through MODULEs and PRIVATE/PUBLIC qualifiers, explicit procedure INTERFACES with INTENT declaration, dynamic allocation of all the data structure for the beam line, the particles and the space charge meshes). Preliminary results of this ongoing work will be presented in this contribution.

## 1 DESCRIPTION OF THE CODE

The code has been developed for the simulation of high current beams in a proton linac with superconducting RF cavities. The chosen independent coordinate is time, expressed in terms of the phase  $\phi = \omega_{RF} t$ , where  $\omega_{RF}$  is  $(2\pi)$  the frequency of the radiofrequency (RF) field. Particle coordinates and momenta are updated in phase steps. If a particle crosses during a timestep two adjacent element boundaries, a substep is performed up to the element end and then the timestep is continued in the

following element. Coordinates at the element output are stored in buffers and written to disk in case phase space plots at given positions in the beamline are desired.

Space charge kicks are applied in phase steps multiple of the particle tracking steps. The space charge kick on each particle can be evaluated either using a direct (point to point) method (with the use of a “screening radius” to prevent the Coulomb divergence of macro particles lying at close distance) or using a fast 3D Poisson solver in the beam frame, based on a multigrid algorithm[1].

### 1.1 Beamline elements

The linac beamline is made of quadrupole, drift space and RF cavity elements. For quadrupoles and drift spaces analytical maps are applied for the evolution during the timestep, whereas in the RF cavities a direct integration of the equations of motion in the space-time dependent cavity electric field is performed.

The RF cavity field is described through an analytical expression of the on-axis longitudinal field of an “ideal  $\beta$  cavity”, as follows:

$$E_z(z, t) = 2E_{acc} \sin(\omega_{RF} t + \phi_c) \sin \frac{\omega_{RF} z}{c\beta_c}$$

where  $E_{acc}$  is the cavity accelerating field,  $\beta_c$  the cavity synchronous velocity and  $\phi_c$  the cavity phase. Thus the energy gain for the synchronous particle with  $\beta = \beta_c$  is  $E_{acc} L$ , where  $L = N \lambda_{RF} \beta_c / 2$  is the active cavity length and  $N$  the number of cells. An iterative preprocessor algorithm (before the actual tracking takes place) sets the cavity phases along the beamline to the desired value for the synchronous phase, defined for the reference particle at the cavity center.

A second order expansion for the off-axis electric and magnetic fields is used. A future extension allowing to use longitudinal electric field maps provided by a cavity eigenfield solver as SUPERFISH[2] is planned.

A special beamline element, providing a uniform focussing channel in the three planes, has also been included in order to check analytical predictions and to test the space charge solver numerical properties with different beam aspect ratios (as discussed in Ref. [3]).

### 1.2 Space charge multigrid implementation

The three dimensional space charge calculation is performed solving the Poisson equation in the rest frame of the synchronous particle (the reference particle). The

electrostatic field in the rest frame is then transformed to the electric and magnetic fields in the laboratory frame, where the space charge kick is applied to the individual particles. The charge distribution on the numerical grid is evaluated in the rest frame using a cloud in cell (CIC) charge assignment scheme, and field interpolation on the particle positions from the grid values uses a trilinear interpolation scheme, for consistency[4].

The Poisson equation for the electrostatic potential is solved on a square mesh, typically consisting of  $33 \times 33 \times 33$  or  $65 \times 65 \times 65$  points (extending to at least 6 rms), using a fast multigrid solver.

Multigrid methods are the fastest iterative methods for the solution of elliptic problems and are based on two main components:

- 1 *standard relaxation algorithms* (as the weighted Jacobi or the Gauss-Seidel)
- 2 the discretization of the model problem on *a series of nested grid levels* (obtained, for example, by step doubling).

The multigrid scheme makes use of the smoothing properties of relaxation schemes: the high frequencies (relative to the grid step) of the error decay by orders of magnitude in the first few iteration of the relaxation operator. However, relaxation is very ineffective for the smooth components of the error (again, the smoothness is to be intended relatively to the grid step).

In a multigrid scheme, relaxation is performed for a few cycles (1-4, typically), to nearly eliminate the fast oscillating errors. After that, only smooth error are left and the estimate of the solution is “restricted” to a coarser level, where a portion of these error components are no longer smooth, due to the step doubling. This process is iterated down the grid levels until reaching the elemental grid consisting of  $3 \times 3 \times 3$  gridpoints (and only one unknown), which can be directly solved. The approximate solutions at each grid level are used then to form a better estimate for the solution on the finer level, through a proper “prolongation” operator. The procedure is then iterated all over the grid hierarchy until the desired convergence is reached. This cycling strategy is known as the V-cycle multigrid scheme and is pictorially illustrated in Figure 1. The V-cycle scheme has a favorable scaling with respect to the grid size, since the number of cycles required in order to converge to a specified residual norm is independent on the dimensions of the finest grid.

The multigrid has been implements in the code using trilinear averaging (known as full-weighting) of the 27 neighboring nodes for the *restriction* operator and trilinear interpolation as the *prolongation* operator. The smoothing operator is the *Gauss-Seidel* algorithm.

Other cycling schemes are possible and were implemented in the code, like the Full Multigrid algorithm[1], but the V cycle allow a simple acceleration mechanism: when using the potential map computed at the previous space charge evaluation the number of

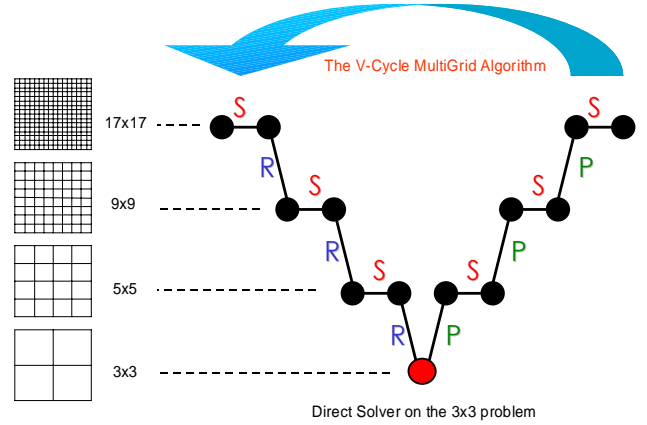


Figure 1: A pictorial representation of the multigrid V-cycling scheme. The S denotes the smoothing operator, R and P denote the restriction and prolongation operators, respectively.

iterations required to converge to the specified norm can be reduced by 30%.

All the multigrid internal routines and data structures are stored in a Fortran 90 Module with PRIVATE attributes and a few PUBLIC interfaces.

### 1.3 Tests and performance of the space charge routine

The space charge solver has been tested both with the results from the direct point to point routine (which can be used with a limited resolution due to the scaling of execution time with the square of the particles number) and with analytical tests. In Figure 2 we show the case of the radial field of a uniformly charged sphere, with a comparison between the analytical solution and the numerical solution of the multigrid routine, interpolated on the position of 10,000 test random positions in the 3D space, in and around the sphere.

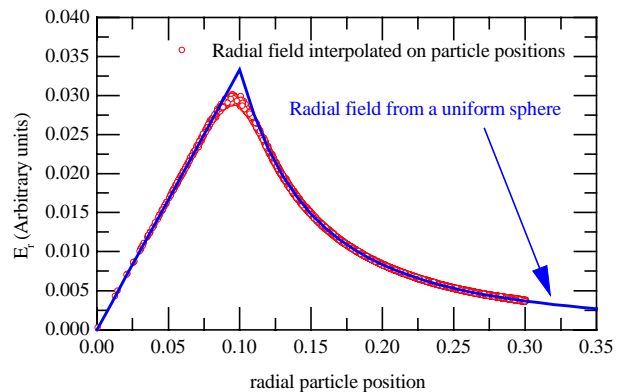


Figure 2: Radial field from a uniformly charged sphere (solid line) and field from the multigrid solver interpolated on the position of 10,000 test positions. The grid extends from -0.5 to 0.5 in x, y, z, the sphere radius is 0.1 and  $33 \times 33 \times 33$  grid points have been used.

Obviously, the numerical solution cannot represent the discontinuous derivative of the exact solution near the sphere edge, due to the charge smoothing on the grid, but is otherwise in excellent agreement with the analytical solution and does not exhibit a directional dependence.

The CPU scaling of the space charge algorithm can be seen from Figure 3, where the time needed for the space charge evaluation (including the charge assignment and the field interpolation) is plotted both with respect to the number of grid points and to the number of particles. Above 100,000 particle most of the execution time is spent in the charge assignment/field interpolation steps, and the space charge step timing is weakly dependent on the finest grid size.

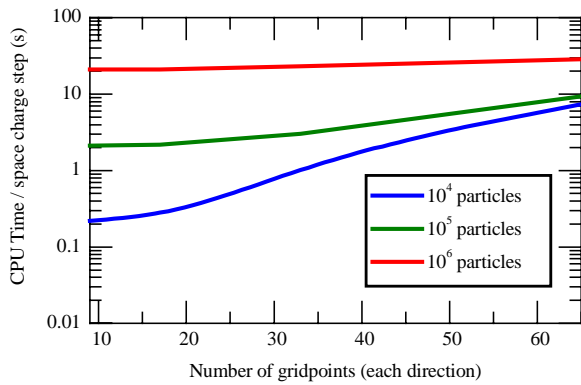


Figure 3: CPU time per space charge step as a function of the number of grid points (on the finest grid) and of the number of particles. Times were measured on a 300 MHz Pentium II 2-processor NT Workstation.

A further improvement for the treatment of the open boundary conditions that allows to increase the mesh resolutions at the beam core by using semi-analytical boundary conditions is currently under test[5].

## 2 THE TRASCO SC LINAC SIMULATIONS

The code has been used to validate the linac design for the superconducting linac of the TRASCO Project[6]. Simulations with up to 100,000 particles have been used for beam dynamics calculations of a 25 mA proton beam in the 100-1600 MeV superconducting accelerator. The linac is split in three sections with five cell elliptical cavities designed for a synchronous  $\beta$  of 0.5, 0.65 and 0.85, grouped in cryostats of 2,3 and 4 structures each.

The matched Twiss beam parameters and the quadrupole and cavity matching parameters between the sections have been determined with adiabatic smooth matching routines that we have implemented in the linear optics code TRACE-3D[7].

Figure 4 shows the rms beam envelopes along the 750 m of the linac beamline. The two section transitions can be clearly identified at approximately 100 and 250 m.

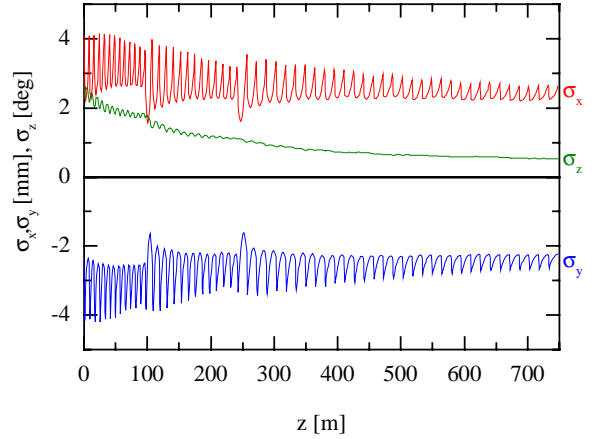


Figure 4: The three rms beam envelopes in the TRASCO linac, matching conditions were determined from TRACE3-D.

Figure 5 shows the horizontal beam size fractions along the linac, normalized by the rms horizontal beam size (in order to get rid of the envelope oscillations in the doublet channel). The curves in the figure refer to the horizontal position containing 90%, 99%, 99.9% and 100% of the beam radius (divided by the horizontal rms beam size). No distribution mismatch can be seen for the whole beam in the first linac section (up to 96 m), where the beam size fractions stay constant, whereas a mismatch in the tails of the distribution is introduced in the transition from the first to the second section. This mismatch is clearly seen by the onset of betatron oscillation from the 99% of the beam and above. The noisy pattern in the 100% curve is due to a poor statistics of the few particles in the outer tail (0.1% of the beam, i.e. only 100 simulation particles).

The simulation used 100,000 particles distributed uniformly in the 6D phase space.

Similar plots can be shown for the other beam profiles (the vertical and the longitudinal), with a distribution mismatch arising from the section transitions.

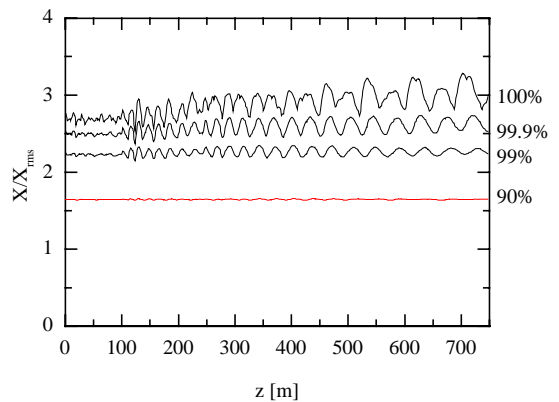


Figure 5: Different horizontal beam ratio profiles along the linac, corresponding to the position containing 90%, 99%, 99.9% and 100% of the beam, divided by the rms value.

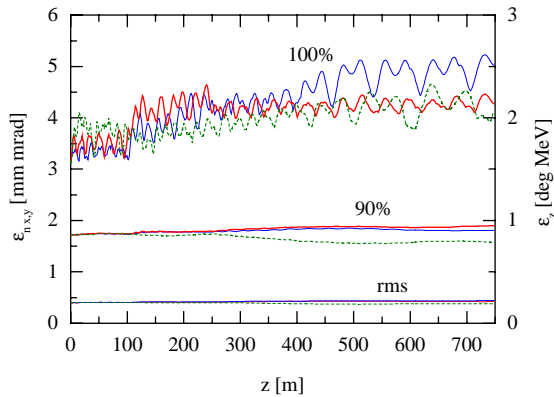


Figure 6: Beam emittances along the linac. Bottom lines are the rms emittances, lines at the middle are the 90% emittances, upper lines are the 100% beam emittances. The longitudinal emittance (to be read on the right axis) is the dashed line, the continuous lines are the horizontal and vertical emittances.

Figure 6 shows the beam emittances along the linac. The figure shows the rms (bottom lines), 90% (intermediate) and 100% (upper lines) beam emittances. No appreciable rms emittance growth can be seen from the plot (when shown in an expanded scale, the rms emittance growth over the whole linac length is limited to well below 10%). An increase of the total emittance at the first transition between the sections can be seen from the plot. This emittance growth at the distribution tails is associated with the distribution mismatch induced by the section transitions.

In Figure 7 the phase space plots at the end of the linac are shown, for the corresponding matched case shown in Figures 3 to 6. Evidences of the beam tails formation in both the longitudinal and transverse planes can be seen from the phase space plots. However, no clear sign of beam filamentation or onset of resonances can be seen from the figure.

Note that the characteristic “rectangular” phase space distribution, corresponding to a moderately tune depressed ( $\nu \approx 0.6$ ) beam, can be seen from Figure 7.

In Figure 8 the same phase space plots at the linac output, as in Figure 7, are shown, for a case where the beam is mismatched in both the horizontal and longitudinal phase spaces. The mismatch factor for this case is 30% (both in the longitudinal and transverse planes). Here, the onset of beam filamentation due to the mismatch can be clearly seen, especially in the longitudinal phase space plane. In this case the rms longitudinal emittance is only 7% higher than the matched case, but the evidence of a strong presence of particles in the beam tails indicates a substantial increase of the total beam emittance.

Simulations with smaller values of the mismatch factors have been performed in order to assess the induced emittance growth. Mismatch factors lower than

10% result in a negligible increase of the rms emittance and a 20% increase of the total (100%) emittances[8].

### 3 CONCLUSIONS

A dedicated tool for the simulation of high current beam dynamics in a superconducting linac has been developed in the framework of the TRASCO Project for a high power linac for nuclear waste transmutation. The code is being used to assist the validation of the linac design and to verify the stringent requirements on beam losses that could cause the linac activation.

A 3D space charge evaluation routine based on an iterative multigrid scheme has been developed and thoroughly tested. The space charge solver efficiency is enough to allow simulations up to 1,000,000 macro particles on a desktop workstation. A future improvement of the code will use parallel processing directives in order to decrease the time consuming space charge evaluation procedures (i.e. the charge smoothing/field interpolation).

The reference design layout for the TRASCO linac has been verified with simulations. No particle losses (with a resolution of 1 to 100,000) have been found, and the emittance growth is limited if the beam mismatch can be controlled to 10%.

For further information on the code and its distribution, please contact the Author[9].

### 4 ACKNOWLEDGEMENTS

I wish to acknowledge the stimulating discussions with all my colleagues of the TRASCO group in Milano-LASA and the contribution of Nicolas Pichoff, from CEA-SACLAY, for the help in the tests of the multigrid algorithm.

### REFERENCES

- [1] ‘A Multigrid Tutorial’, by Briggs, William, published by SIAM, Philadelphia, PA 1987, ISBN 0-89871-221-1, and ‘An Introduction to Multigrid Methods’, by Wesseling, Pieter, published by John Wiley and Sons, New York, 1992, ISBN 0-471-93083-0.
- [2] ‘POISSON/SUPERFISH’, by Billen, James and Young, Lloyd, LA-UR-96-1834, Los Alamos, NM, 1996.
- [3] ‘Simulation Results with an Alternate 3D Space-Charge Routine, PICNIC’, Pichoff, N, Lagniel, J M, Nath, S, in Proceedings of the XIX International Linear Accelerator Conference, August 23-28 1998, Chicago, IL.
- [4] ‘Computer Simulations Using Particles’, by Hockney, R W and Eastwood, J W, published by Adam Hilger, New York, NY 1988, ISBN 0-85274-392-0.
- [5] Nicolas Pichoff, CEA Saclay, private communication.
- [6] ‘Status of the INFN High Current Proton Linac for Nuclear Waste Transmutation’, Pagani, C, Barni, D, Bellomo, G, Parodi, R, Pierini, P, in Proceedings of the XIX International Linear Accelerator Conference, August 23-28 1998, Chicago, IL.
- [7] TRACE3-D Documentation, Krandall, K, Rushtoi, D, LA-UR-97-886, Los Alamos, NM, 1987.
- [8] ‘Beam Dynamics in a High Current SC Proton Linac for Nuclear Waste Transmutation’, Bellomo, G, Pierini, P, in Proceedings of the XIX International Linear Accelerator Conference, August 23-28 1998, Chicago, IL.
- [9] The Author can be contacted by e-mail with the following address: Paolo.Pierini@mi.infn.it

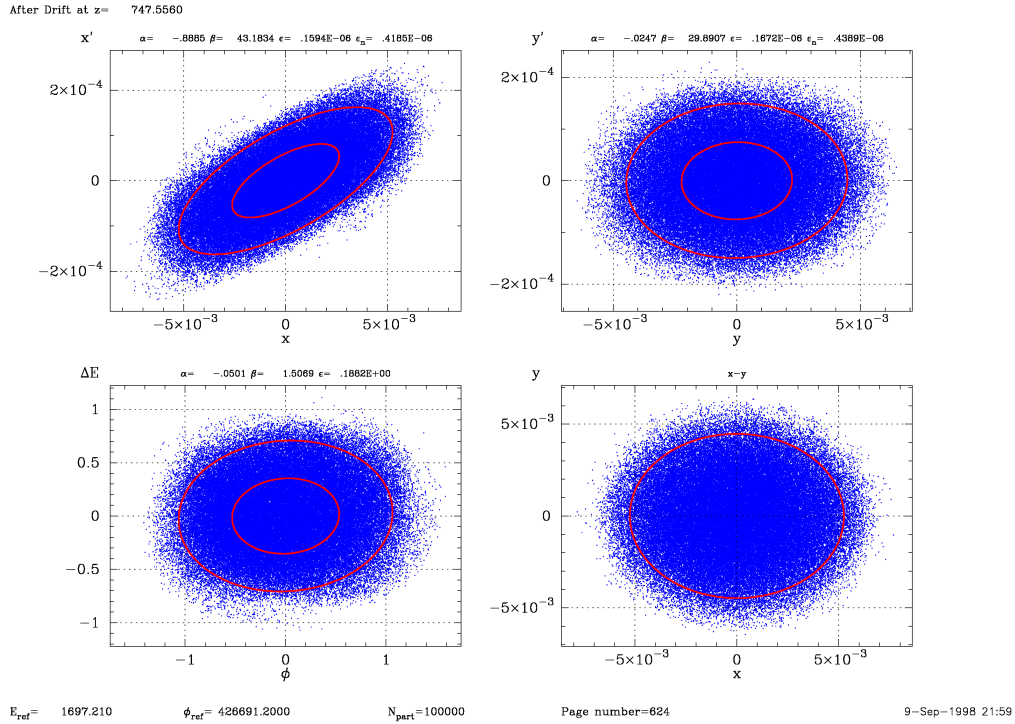


Figure 7: Phase space plots at the linac end (1.7 GeV after 750 m of linac). Upper left: horizontal plane, Upper right: vertical plane, Bottom left: longitudinal plane, Bottom right: transverse distribution. Units are m and rad for the transverse planes and deg MeV for the longitudinal. Reference case for the “adiabatically matched” beam. The ellipses shown in the phase space plots represent the rms emittance and 4 times the rms value.

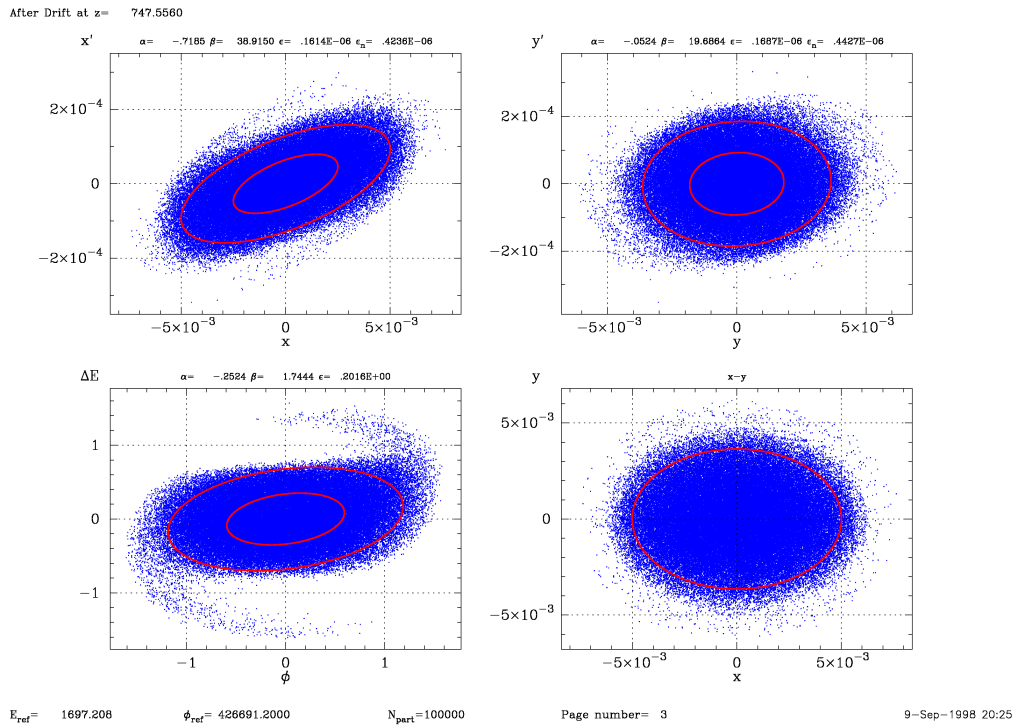


Figure 8: Same case for Figure 7 at the linac output, but for an initially mismatched beam (with a longitudinal and transverse mismatch factor of 30%).